

Models of non-Boussinesq lock-exchange flow

R. ROTUNNO¹†, J. B. KLEMP¹, G. H. BRYAN¹
AND D. J. MURAKI²

¹National Center for Atmospheric Research, Boulder, CO 80307, USA

²Department of Mathematics, Simon Fraser University, Burnaby, BC V5A 1S6, Canada

(Received 30 April 2010; revised 7 October 2010; accepted 16 December 2010;
first published online 8 April 2011)

Nearly all analytical models of lock-exchange flow are based on the shallow-water approximation. Since the latter approximation fails at the leading edges of the mutually intruding fluids of lock-exchange flow, solutions to the shallow-water equations can be obtained only through the specification of front conditions. In the present paper, analytic solutions to the shallow-water equations for non-Boussinesq lock-exchange flow are given for front conditions deriving from free-boundary arguments. Analytic solutions are also derived for other proposed front conditions – conditions which appear to the shallow-water system as forced boundary conditions. Both solutions to the shallow-water equations are compared with the numerical solutions of the Navier–Stokes equations and a mixture of successes and failures is recorded. The apparent success of some aspects of the forced solutions of the shallow-water equations, together with the fact that in a real fluid the density interface is a free boundary, shows the need for an improved theory of lock-exchange flow taking into account non-hydrostatic effects for density interfaces intersecting rigid boundaries.

Key words: gravity currents, shallow water flows, turbulence simulation

1. Introduction

Lock-exchange flow results from the adjustment under gravity of two fluids of different densities initially separated by a vertical partition in a horizontal channel (figure 1*a*) and is a prominent feature of natural flows and engineering applications (see e.g. Lowe, Rottman & Linden 2005, p. 102, referred to as LRL). In addition to the gravity and pressure-gradient forces, a model of lock-exchange flow must deal with stress at the channel walls, stress and diffusion between the two fluids and in cases involving a liquid–gas interface, surface-tension effects. Given the mathematical complexity attached to these processes, the more tractable two-layer shallow-water equations, in which the aforementioned processes are either neglected or simply represented, have been applied to lock-exchange flow by Rottman & Simpson (1983, referred to as RS), Keller & Chyou (1991), Klemp, Rotunno & Skamarock (1994, referred to as KRS), Shin, Dalziel & Linden (2004), LRL and Ungarish (2007, 2008, 2010). Judging the relative merits of these differing applications of the shallow-water equations against laboratory data is difficult owing to the influence of the aforementioned neglected effects. However, the gap between the shallow-water theory and laboratory experiments can be bridged in certain cases by using numerical

† Email address for correspondence: rotunno@ucar.edu

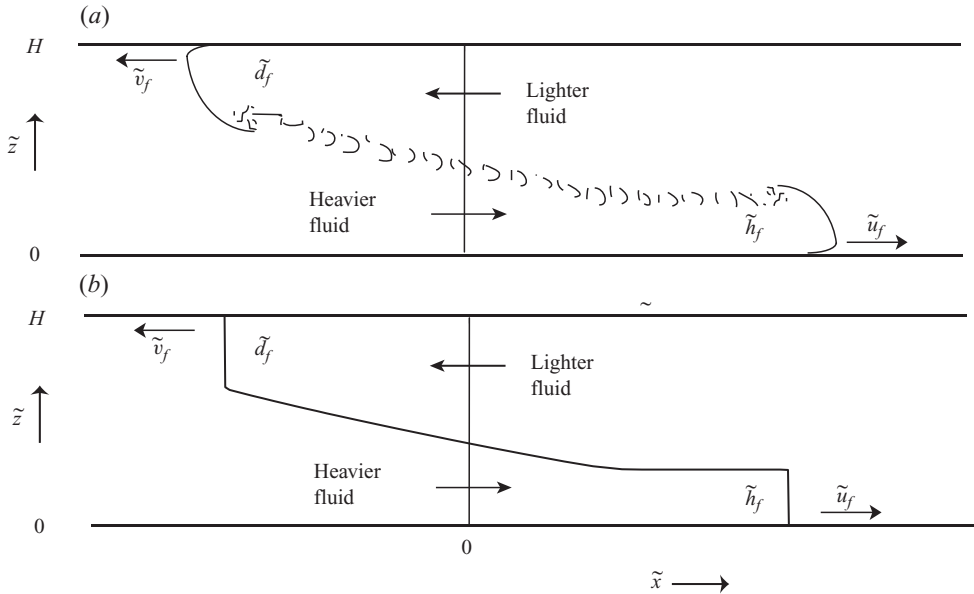


FIGURE 1. Schematic of lock-exchange flow based on (a) laboratory data, and (b) typical solutions to the shallow-water equations. The vertical line at $\tilde{x} = 0$ indicates the lock centre where the heavier and lighter fluids are initially separated; the horizontal channel walls are separated in the vertical by a distance H . After the release of the lock the heavier (lighter) fluid flows to the right (left) at speed \tilde{u}_f (\tilde{v}_f) with thickness \tilde{h}_f (\tilde{d}_f) measured some distance behind the complicated flow at the leading edge.

integrations of less approximate fluid-flow equations as surrogates for laboratory data as in KRS and Birman, Martin & Meiburg (2005). In this article, we extend the Boussinesq (density ratio of lighter to heavier fluid $r \approx 1$), two-layer shallow-water theory put forward by KRS to the non-Boussinesq case and then evaluate it and another shallow-water theory against compatible (i.e. free-slip, no surface-tension, etc.) numerical integrations of the Navier–Stokes (NS) equations for lock-exchange flow.

As the shallow-water equations (SWE) are based on the hydrostatic approximation, they are incapable of describing flow with strong horizontal variation such as at the leading edges of the mutually intruding interfaces shown in figure 1(a). In order to use the SWE in such cases, one admits solution discontinuities and appeals to a more complete physical theory for conditions that apply across them. RS proposed using a formula developed by Benjamin (1968, his (2.22)) to relate the right-moving front speed \tilde{u}_f to its depth \tilde{h}_f in a Boussinesq ‘dam-break’ calculation using the two-layer SWE. Benjamin’s formula, based on the mass and momentum balance across a control volume moving with a steadily propagating ‘gravity current’ (e.g. Ungarish 2009, chapter 3), gives \tilde{u}_f in terms of the height \tilde{h}_f of the lower fluid well behind the complex flow of the gravity-current head; in solutions of the SWE, Benjamin’s control volume containing the gravity-current head is represented by a simple discontinuity as shown in figure 1(b). In their application of the two-layer SWE to the Boussinesq lock-exchange problem, RS found that the left-moving interface (figure 1a), which was left to evolve freely, immediately became multi-valued (see figure 7c of RS). KRS resolved the latter problem by recognizing that the left-moving interface must also be represented by a discontinuity that satisfies Benjamin’s front condition (figure 1b);

figure 7(d) of KRS gives the numerical solution of the SWE for the lock-exchange problem in the Boussinesq limit. Recently, an analytical solution for the latter case has been derived by Ungarish (2010, see Appendix).

A continuing source of discussion in the literature is that the Benjamin front condition admits a special dissipation-free solution along with a continuum of solutions having dissipation (e.g. Ungarish 2008). KRS pointed out that the dissipation-free front condition in the SWE would imply a front speed that is greater than the speed at which information can travel to it from the lock centre (violating ‘causality’) in both the Boussinesq ($r \approx 1$) and cavity ($r \rightarrow 0$) limits (see figure 3 of KRS). On the other hand, some laboratory investigators promote the relevance of the dissipation-free front condition to experimental flows (e.g. Shin *et al.* 2004), while other laboratory experiments (Simpson & Britter 1979) and numerical experiments (Härtel, Meiburg & Necker 2000; Bryan & Rotunno 2008) find flows consistent with a dissipative front condition for Boussinesq lock-exchange flow. For non-Boussinesq conditions ($r < 1$), laboratory experiments (Keller & Chyou 1991; Gröbelbauer, Fannelop & Britter 1993; Lowe *et al.* 2005) and numerical simulations (Birman *et al.* 2005; Étienne, Hopfinger & Saramito 2005; Bonometti, Blachandar & Magnaudet 2008) show that as r decreases from unity, the right-moving front of the relatively heavy fluid increases in speed and becomes more turbulent, while the speed of the left-moving front of relatively light fluid remains unchanged and becomes less turbulent.

This latter feature led Keller & Chyou (1991) to consider the left-moving front as the realization of the dissipation-free Benjamin front condition. Following Keller & Chyou (1991), LRL used two-layer shallow-water theory to construct the solution between the dissipation-free left-moving upper front and a right-moving front obeying the (generally dissipative) Benjamin front condition across the range of r (figure 4b of LRL). The ‘causality’ problem raised by KRS of the impossibility of information flow in the SWE from lock centre to the dissipation-free front was not addressed.

In the present paper, we extend the KRS Boussinesq two-layer shallow-water theory to apply across the range of r . As in KRS, the present theory is based on the two-layer SWE and the application of the Benjamin front condition to the left- and right-moving fronts, respectively. As with the KRS numerical integrations of the SWE in the Boussinesq limit, the present non-Boussinesq solutions require the dissipative Benjamin front condition across the range $0 < r \leq 1$ for solutions that obey causality. We then verify that these numerical solutions are unique through an independent exact analysis using the method of characteristics. For comparison with the present solutions, we have also constructed analytical solutions following the LRL approach described above. The exact solutions given herein offer a mathematically firm explanation for the numerical-solution features such as the ‘expansion fans’ and ‘zones of constant state’ that appear in them. Perhaps more important is that the exact analysis gives a clear picture of information flow through the system as seen by the shallow-water theory.

To evaluate the present and the LRL SWE solutions, we have carried out two- and three-dimensional numerical simulations using the NS equations. The simulations are carried out under free-slip conditions at the channel walls and without surface-tension effects. One effect contained in the NS equations but not in the SWE is interfacial instability; hence turbulent exchanges of mass and momentum between layers are unavoidable as they effect the growth and ultimate disposition of unstable waves growing on the interface. As pointed out by Benjamin (1968, pp. 224–225), the upper gravity current is completely stable as $r \rightarrow 0$ while it is unstable as $r \rightarrow 1$; on the other

hand, the lower gravity current is unstable at any r . Consistent with the foregoing arguments, the present numerical solutions indicate that the character (laminar or turbulent) of the upper front is a function of both r and the relative strength of turbulent exchanges through the Reynolds number Re . For Re greater than some threshold that depends on r , we find better agreement between the NS solutions with the present extension of the KRS theory than with the LRL theory; however for Re less than that threshold, the numerical solutions indicate better agreement with the LRL theory than with the present one.

Hence, we are led to the conclusion that for relatively smaller Re , the solution to the NS equations for the lock-exchange problem is outside the SWE solution space for solutions respecting the causality condition. Our exact analysis of the LRL SWE solutions indicates that all information flows from the left-moving dissipation-free front inward towards the lock centre. From the point of view of the SWE, the left-moving front must thus be viewed as an external agent; that is, the mathematical problem becomes a forced- (rather than a free-) boundary problem.

Numerical solutions of two-layer SWE for non-Boussinesq lock-exchange flow are described next in §2. Motivated by these numerical solutions, which are consistent with information flow from the lock centre outward, §3 describes an exact ‘causal’ analytical solution to SWE using the method of characteristics. In the review process, it was discovered that M. Ungarish and the authors had independently arrived at the same SWE solutions; the reader is referred to Ungarish (2011) for his derivation which also treats the case of ‘partial-depth release’. For reasons listed above, we also give in §3, analytical solutions of the SWE for prescribed frontal parameters at the left-moving front of lighter fluid; these solutions do not respect ‘causality’ but may nonetheless be useful descriptions of fluid flow features that are beyond shallow-water theory. In §4 the SWE solutions are compared to those of the less-approximate NS equations and, in particular, the variation of the solutions with both density ratio r and Re is examined. A summary and concluding remarks are given in §5.

2. Numerical solution of the two-layer shallow water equations

Following RS, Keller & Chyou (1991) and LRL, the two-layer SWE equations for flow in a horizontal channel neglecting stress, diffusion and surface tension, can be written in terms of the lower-layer height and velocity; in non-dimensional form these are

$$\frac{\partial h}{\partial t} + u \frac{\partial h}{\partial x} + h \frac{\partial u}{\partial x} = 0 \quad (2.1)$$

and

$$\frac{\partial u}{\partial t} + a \frac{\partial u}{\partial x} + b \frac{\partial h}{\partial x} = 0, \quad (2.2)$$

where

$$a = u \frac{(1-h)^2 - rh(1+h)}{(1-h)^2 + rh(1-h)} \quad \text{and} \quad b = \frac{(1-h)^3 - ru^2}{(1-h)^3 + rh(1-h)^2}. \quad (2.3a, b)$$

In (2.1)–(2.3), $h = \tilde{h}/H$ and $u = \tilde{u}/\sqrt{g'H}$, where \tilde{h} is the depth and \tilde{u} the velocity, of the lower layer; the independent variables are $x = \tilde{x}/H$ and $t = \tilde{t}/\sqrt{g'H}$; the reduced acceleration due to gravity is defined by $g' = (1-r)g$. For future reference, note that $d = \tilde{d}/H = 1-h$ and, by continuity, $v = \tilde{v}/\sqrt{g'H} = -uh/d$, where v is the velocity and d is the depth of the upper layer. The initial condition is $u(x, 0) = 0$ and $h(x, 0) = 1$ for $x \leq 0$ and $h(x, 0) = 0$ for $x > 0$.

As mentioned in the Introduction, RS used a front condition to represent the gravity current at the leading edge of the right-moving fluid in a Boussinesq shallow-water calculation, while the left-moving intrusion was left to evolve freely. As evidenced by the result of that calculation (figure 7c of RS), $h(x, t)$ for the left-moving interface immediately became multi-valued for $t > 0$. KRS demonstrated, through an evaluation of the wave-propagation characteristics at the leading edge of the disturbance propagating to the left into a reservoir of depth h (where $0 < h \leq 1$ with $h = 1$ representing lock-exchange flow), that deeper heights travel slower than shallower heights for $h > 0.5$; hence multi-valued solutions are to be expected, and the application of a front condition is required for Boussinesq lock-exchange flow. For the present non-Boussinesq case, the wave speeds associated with the system (2.1)–(2.2) are given by

$$c^\pm(u, h) = \frac{1}{2}(u + a) \pm \frac{1}{2}\sqrt{(u + a)^2 - 4(au - bh)} \quad (2.4)$$

(equation (3.13) of LRL); setting $u = 0$ in (2.4) gives

$$c^- \approx -\sqrt{\frac{h(1-h)}{1-(1-r)h}}, \quad (2.5)$$

for a disturbance propagating to the left into a reservoir of height h . Following KRS, one can deduce that lower heights travel faster than higher heights for $h > (1 + \sqrt{r})^{-1}$. In the Boussinesq limit, $r = 1$ and KRS's result is recovered showing that lower heights travel to the left faster than higher ones for $h > 0.5$. The present analysis of (2.5) shows that lower heights travel faster than higher heights for any finite $r \neq 0$ and hence there is the necessity for a front condition for lock-exchange flow ($h = 1$); for a fuller discussion of this point see Ungarish (2011). We note in passing that (2.5) illustrates just one of the many intricacies associated with a *moving contact line* (Shikhmurzaev 2008, chapter 5). In the foregoing argument we are first considering the limit $h \rightarrow 1$ (lock exchange) and then $r \rightarrow 0$ (cavity). However, had we first taken $r \rightarrow 0$, (2.5) would then have given the classical one-layer result $c^- = -\sqrt{h}$, implying that the lower fluid takes no notice of the upper fluid, and therefore, of the upper bounding surface, even in the limit $h \rightarrow 1$.

Following Benjamin (1968), application of mass and momentum conservation across the front of each gravity current gives

$$v_f = -\sqrt{\frac{d_f(2-d_f)(1-d_f)}{1+d_f}} \equiv -\mathcal{B}(d_f), \quad (2.6)$$

for the left-moving front, and

$$u_f = \sqrt{\frac{1}{r} \frac{h_f(2-h_f)(1-h_f)}{1+h_f}} = \sqrt{\frac{1}{r}} \mathcal{B}(h_f), \quad (2.7)$$

for the right-moving front.

Numerical solutions to (2.1)–(2.2) are computed using a simple leapfrog time integration with second-order centred spatial differencing on a staggered C grid. The equations are integrated over the range x_L to x_R , where x_L and x_R are the locations of the left- and right-moving fronts, respectively. At each front, (2.1) is integrated using one-sided spatial differences, and the velocities are specified from the Benjamin front condition (2.6) or (2.7). The positions x_L and x_R of the fronts are advanced each time step using the frontal velocities (2.6) and (2.7).

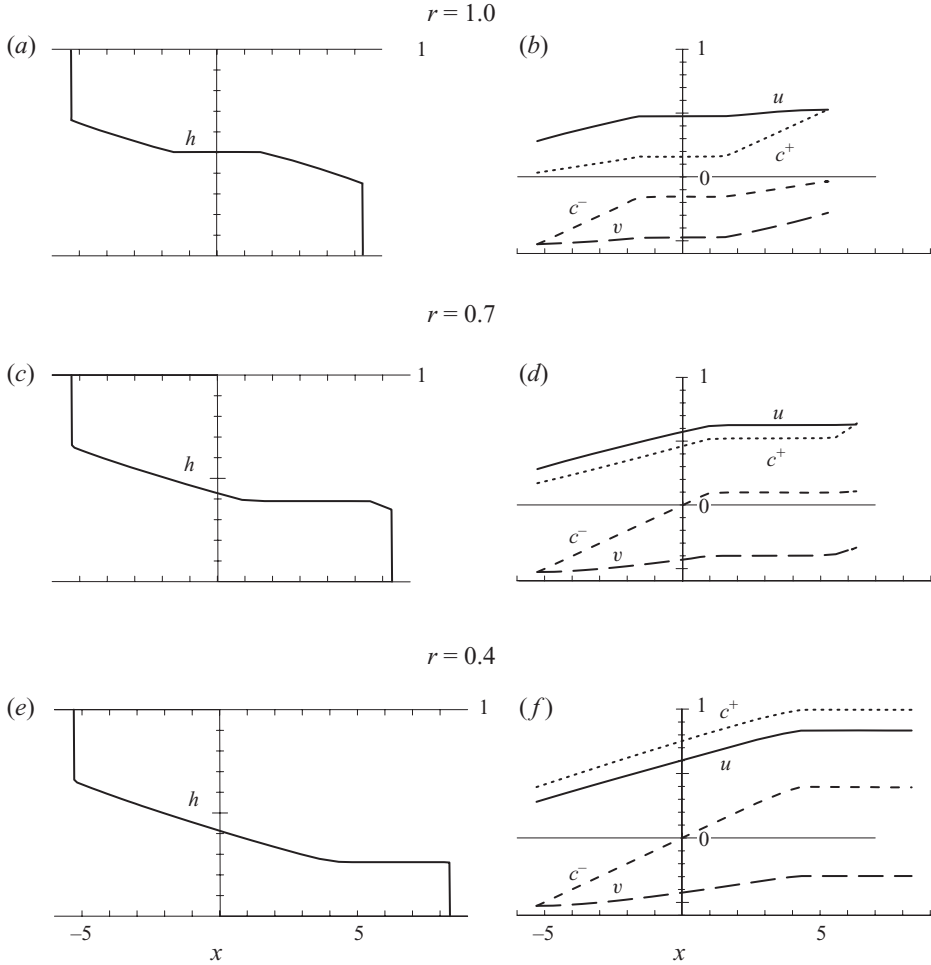


FIGURE 2. Numerical solutions of the two-layer shallow water equations with the front conditions (2.6)–(2.7) for $r=1.0, 0.7$ and 0.4 . For each r , the height of the interface is displayed in (a), (c) and (e), and the layer velocities and wave speeds (2.4) are displayed in (b), (d) and (f).

The numerical solutions are shown in figure 2 for $r=1.0, 0.7$ and 0.4 . Figures 2(a), 2(c) and 2(e) show snapshots at $t=10$ of the interface height $h(x)$, while figures 2(b), 2(d) and 2(f) show the corresponding velocities $u(x)$ and $v(x)$ in the lower and upper layers, respectively. For the Boussinesq case (figure 2a,b), the solution has the required reflective symmetry [$h(x)=d(-x)$, $u(x)=-v(-x)$]; the frontal parameters, $h_f=d_f=0.3473$ and $u_f=-v_f=0.527$ (cf. KRS's figure 7d). For the density ratio $r=0.7$, figure 2(c) indicates that $h(x)$ is no longer symmetric, although the front heights are still equal to their values in the $r=1$ case (figure 2a). Moreover, the velocity distributions (figure 2d), indicate that the lower-fluid front speed has increased, while that of the upper fluid has remained as it was in the $r=1$ case (figure 2b). With the density ratio reduced to $r=0.4$, figure 2(e) indicates no change in the thickness d_f of the left-moving front, while that of the right-moving front h_f is reduced, with respect to the $r=1.0$ and 0.7 cases; the velocity distributions in figure 2(f) indicate a further speed increase of the right-moving front, but no change in that of the left-moving

front. In contrast with the $r = 1.0$ and 0.7 cases, the case with $r = 0.4$ has both h and u independent of x for some distance behind the right-moving front.

To aid in the interpretation of the numerical solutions shown in figure 2, we examine the corresponding wave speeds $c^\pm(u, h)$ given by (2.4). Figure 2(b) shows for the $r = 1.0$ case that $0 < c^+ \leq u$ and, by symmetry, $v \leq c^- < 0$. With the density ratio $r = 0.7$, figure 2(d) shows that, as in the case with $r = 1.0$, $0 < c^+ \leq u$ but that c^+ is closer in magnitude to u throughout the interval between the fronts. On the other hand for c^- , figure 2(d) for $r = 0.7$ shows that $v \leq c^- \leq 0$ for $x \leq 0$ and that $c^- \geq 0$ for $x \geq 0$, indicating that no information can travel from the right to the left of $x = 0$. At a density ratio of $r = 0.4$, figure 2(f) shows that $c^+ > u$, while the distribution of c^- is qualitatively the same as for the $r = 0.7$ case.

3. Solutions of the SWE by the method of characteristics

The lock-exchange problem shares with the classic dam-break and (constant velocity) piston problems, the property that the governing equations, front conditions and the initial conditions are without any implied space or time scales (Whitham 1974, p. 191). For $t > 0$, the solution has a form known as a simple wave and can only depend on the similarity variable x/t , so that the time evolution is simply a linear-in-time dilatation of the spatial structure. In this section, this spatial profile is determined by the method of characteristics.

The hyperbolic equations (2.1)–(2.2) can be written as

$$\begin{pmatrix} h \\ u \end{pmatrix}_t + \begin{bmatrix} u & h \\ b & a \end{bmatrix} \begin{pmatrix} h \\ u \end{pmatrix}_x = \mathbf{0}, \quad (3.1)$$

where the wave speeds c^\pm (2.4) are obtained as the eigenvalues of the matrix. Multiplication by the left eigenvector $(a - c^\pm, -h)$ gives the Riemann invariant relation

$$(a - c^\pm) \frac{dh}{dt} - h \frac{du}{dt} = 0, \quad (3.2)$$

where the derivatives are along characteristic trajectories (or ‘rays’) defined by $dx^\pm/dt = c^\pm$ (Whitham 1974, p. 116). As the Riemann invariant relation has no explicit dependence on x or t , it can be integrated as the ordinary differential equation:

$$\frac{du}{dh} = \frac{a - c^\pm(u, h)}{h}, \quad (3.3)$$

giving a relation between u and h along rays $x^\pm(t)$ (Courant & Friedrichs 1948, p. 44). In the present application, we will be concerned with two specific solutions of (3.3); these are the inbound rays launched from each of the two fronts. We define $u^+(h)$ using (3.3) with the $c^+(u, h)$ wave speed and starting values given by the left-moving frontal parameters (u_L, h_L) . Likewise, we define $u^-(h)$ with the $c^-(u, h)$ wave speed initialized with the right-moving frontal parameters (u_R, h_R) . This set-up for the method of characteristics is the same as described in Ungarish (2009, chapter 2) and the Boussinesq analysis of Chumakova *et al.* (2009).

3.1. Free-boundary front conditions

The locations of the left- and right-moving fronts that delimit the propagation of the lock-exchange flow into the quiescent fluid are determined here by free-boundary arguments. Conservation of mass dictates that the fronts move with the fluid speed; hence, on a ray diagram, the right-moving front is the event line $x/t = u_R$, and

the left-moving front is the event line $x/t = v_L$. The assumption of the Benjamin relation provides one condition: $\sqrt{r} u_R = \mathcal{B}(h_R)$ (2.7) for the right-moving front, and $v_L = -\mathcal{B}(d_L)$ (2.6) for the left-moving front. However, determination of both frontal variables, (u_R, h_R) , or (v_L, d_L) , requires a second front condition. An assumption of causality leads to two distinct scenarios for this second condition, and we refer to these cases as the *characteristic Benjamin front* and the *time-like Benjamin front*. These are discussed below, where the right-moving front is considered first.

3.1.1. Right-moving front specifications

The assumption of causality requires that this front propagates no faster than the right-going characteristic speed ($u_R \leq c_R^+$), yet also influences the region of fluid behind it ($c_R^- < u_R$). Hence,

$$c_R^- < u_R \leq c_R^+ \quad (3.4)$$

but two cases emerge depending on whether the front intersects the c^+ -characteristics ($u_R < c_R^+$) or itself is a characteristic ($u_R = c_R^+$). The latter situation defines the characteristic Benjamin front, where the event line coincides with a right-going c^+ -ray – as occurs in the classic ‘dam-break’ problem (Whitham 1974, p. 457). The second front condition is then

$$u_R = c_R^+ = c^+(u_R, h_R). \quad (3.5)$$

It follows from the characteristic equation (2.4) that (3.5) is satisfied only when $b(u_R, h_R) = 0$, so that from (2.3b),

$$r u_R^2 = (1 - h_R)^3. \quad (3.6)$$

Simultaneous solution of (3.6) with the Benjamin front condition (2.7) gives the unique specification

$$\sqrt{r} u_R \approx 0.5273, \quad h_R \approx 0.3473, \quad (3.7)$$

for the frontal parameters. It may be verified from (2.4) that for frontal parameters (3.7), $c_R^- < u_R$, as required by (3.4).

The time-like Benjamin front is defined by the situation of strict inequality

$$c_R^- < u_R < c_R^+, \quad (3.8)$$

where the front now intersects c^+ -rays – as occurs in the well-known ‘piston’ problem (Whitham 1974, p. 164). The second front condition is obtained from the Riemann invariant that originates from the left-moving front, so that $u_R = u^+(h_R)$ as obtained by the solution of (3.3).

3.1.2. Left-moving front specifications

Considering now the left-moving front, the causality inequality analogous to (3.4) is

$$c_L^- \leq v_L < c_L^+. \quad (3.9)$$

A left-moving characteristic Benjamin front is thus defined by the equality

$$v_L = c_L^- = c^-(u_L, h_L), \quad (3.10)$$

which gives the second front condition. Following the same logic for deriving (3.6), the condition (3.10) leads to the relation

$$v_L^2 = (1 - d_L)^3. \quad (3.11)$$

For the left-moving characteristic front then, combining (3.11) with the Benjamin front condition (2.6) gives the numerical solution for the frontal parameters:

$$v_L \approx -0.5273, \quad d_L \approx 0.3473, \quad (3.12)$$

where these r -independent values match those of the symmetric Boussinesq case (Ungarish 2009, 2010). The corresponding values for the lower fluid are

$$u_L \approx 0.2806, \quad h_L \approx 0.6527. \quad (3.13)$$

There is also the possibility for a left-moving time-like Benjamin front. However, our numerical SWE solutions, like those shown in figures 2(d) and 2(f), suggest that $c_L^- = v_L$ is the only outcome. The impossibility of a left-moving time-like front leads to the proof for the uniqueness of causal solutions at the close of this section.

3.2. Free-boundary causal solutions

3.2.1. Boussinesq case, $r = 1$

We are now ready to construct solutions to the SWE by the method of characteristics and begin with the Boussinesq case ($r = 1.0$). Consistent with figure 2(a), we assume that both left- and right-moving fronts are of the characteristic Benjamin type so that the region of disturbed flow on a ray diagram lies inside the cone $c_L^- \leq x/t \leq c_R^+$. The heavy solid curves in figure 3(a) shows the two Riemann invariants, $u^\pm(h)$, as obtained by numerical solution of (3.3). The invariant $u^-(h)$ originates from the right-moving front, as specified by the initial conditions $u^-(h_R) = u_R$ (3.7) and corresponds to the left-going rays. Likewise, $u^+(h)$ originates from the left-moving front, as specified by the initial conditions $u^+(h_L) = u_L$ (3.13) and corresponds to the right-going rays. There is a unique crossing point at $h_c = 0.5$, where $u^+(h_c) = u^-(h_c) = u_c \approx 0.4746$. These are values for a ‘zone of constant state’ that is the only condition under which both the Riemann invariant conditions are satisfied. This intersection defines three cones of influence. The rays from the right-moving front influence the region $c_c^- \leq x/t \leq c_c^+$, while the left-moving front influences the region $c_L^- \leq x/t \leq c_c^+$, where $c_c^- = c^-(u_c, h_c)$ and $c_c^+ = c^+(u_c, h_c)$. These overlapping cones of influence define the third region, $c_c^- \leq x/t \leq c_c^+$, of constant state. Referring to figure 4(a), the upper panel illustrates this constant state (thin line segment) in terms of $h(x/t)$, with the overlap region $c_c^- \leq x/t \leq c_c^+$ in the ray diagram directly below. The non-overlapping regions are influenced by only one of the frontal rays and by the theory of simple waves, must be expansion fans. The values of $h(x/t)$ of the left-side fan, $v_L \leq x/t \leq c_c^-$, can be deduced parametrically from

$$x/t = c^-[u^+(h)], \quad (3.14)$$

where $c^-[u^+]$ is defined by the values on the so-labelled curve in figure 3. Likewise, the right-side fan, $c_c^+ \leq x/t \leq u_R$, is given by

$$x/t = c^+[u^-(h)]. \quad (3.15)$$

The solution $h(x/t)$ for these two expansion fans is shown by the thick line segments in the upper panel of figure 4(a) – and matches the symmetric Boussinesq solution of Ungarish (2010, see Appendix). In addition, we have confirmed that our numerically computed characteristic wave speeds satisfy $3c^\pm - c^\mp$, to be constant along c^\pm -rays (Chumakova *et al.* 2009). Finally, the rays are computed numerically using $dx^\pm/dt = c^\pm$ with (3.7) or (3.13) and shown as thin lines in the lower panel of figure 4(a). It may be verified that the analytical solution for $h(x/t)$ shown in figure 4(a) is essentially identical to the SWE numerical solution shown in figure 2(a).

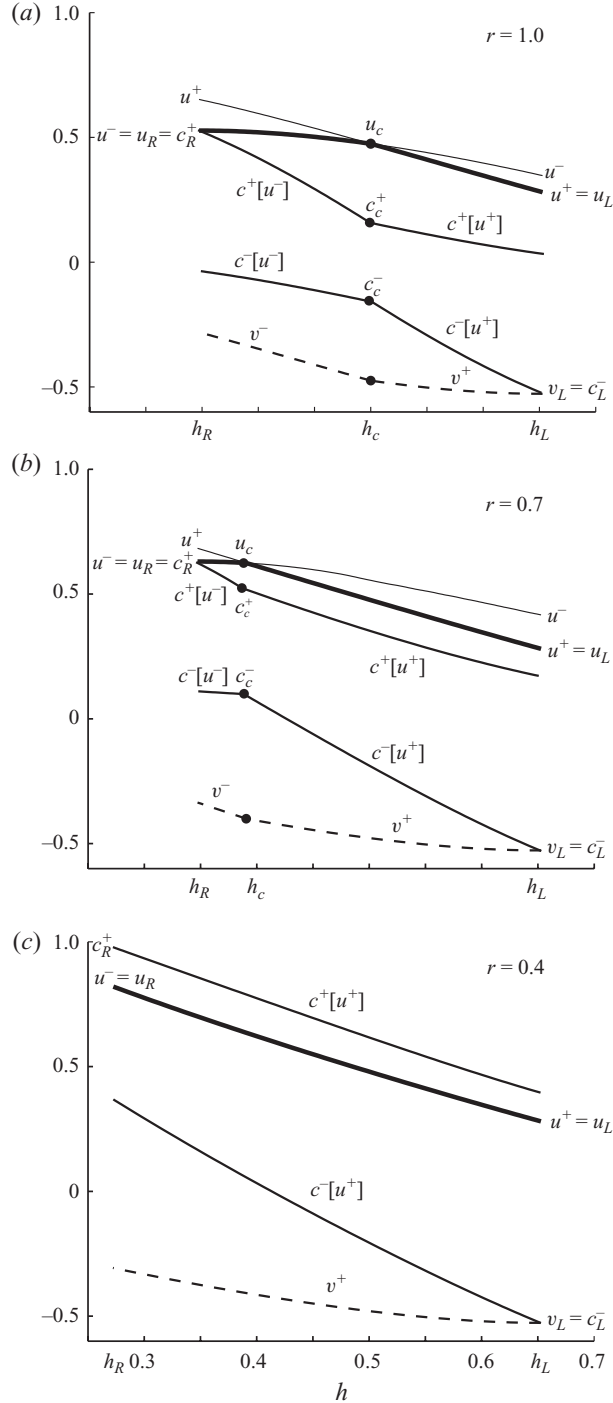


FIGURE 3. Solution to the Riemann invariant equation (3.3) for $u^\pm(h)$ for density ratios $r = (a)$ 1.0. (b) 0.7 and (c) 0.4. Starting values for the integrations of (3.3) are indicated by the points $u^- = u_R, h = h_R$ and $u^+ = u_L, h = h_L$. In (a) and (b) , (u_c, h_c) denotes the crossing point where $u^+(h) = u^-(h)$ and the thick solid lines indicates the parts of the $u^\pm(h)$ solution curves relevant for calculating the corresponding wave speeds $c^\pm[u^\pm]$, $c^\pm[u^-]$ and upper-layer velocities v^\pm (long-dashed curves). In (c) there is no crossing point which indicates a change in character of the solution.

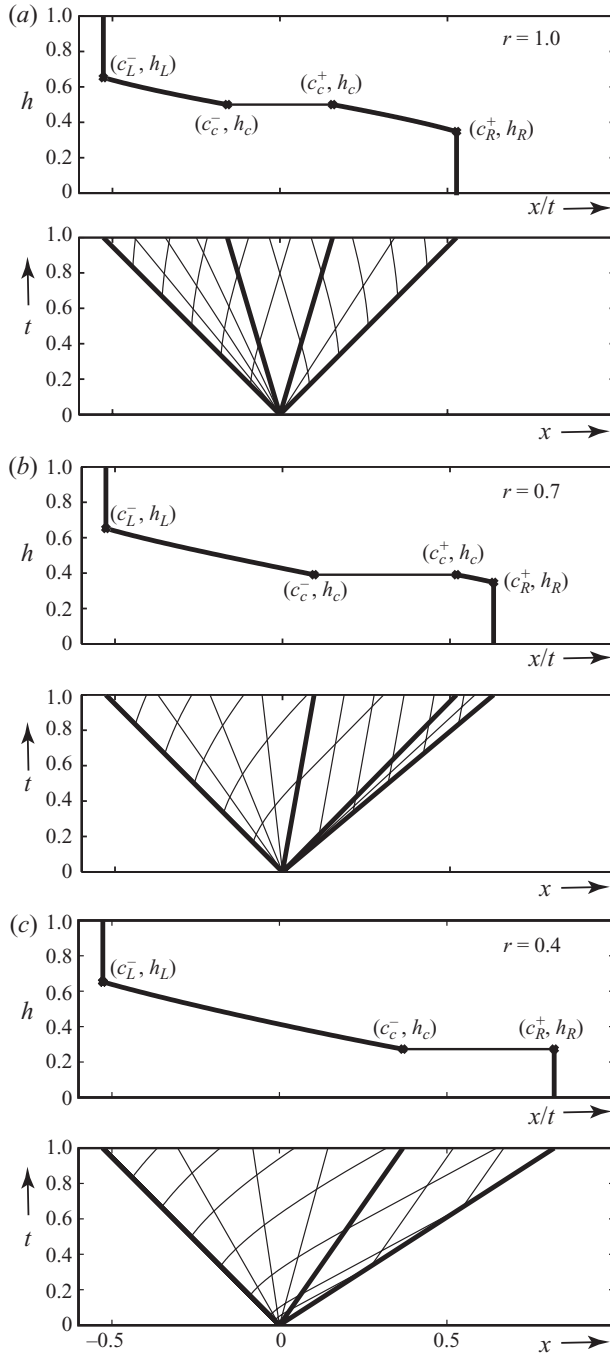


FIGURE 4. Analytical construction of the solution to the shallow water equations for density ratios $r = (a)$ 1.0, (b) 0.7 and (c) 0.4. For each case the height of the interface h (upper panel) is plotted versus the combined coordinate x/t with the corresponding ray diagram given directly below. In (a) and (b) the zone of constant state where $h(x/t) = h_c$ (thin line segment) is located within the cone $c_c^- < x/t < c_c^+$ indicated in the ray diagram, and the left and right-side expansion fans (thick line segments) are defined by the ray-diagram cones $c_L^- < x/t < c_c^-$ and $c_c^+ < x/t < c_R^+$, respectively. In (c) the right-side expansion fan disappears.

3.2.2. Non-Boussinesq case, $r = 0.7$

Following the same procedure as for the Boussinesq case, we next construct the solution for the non-Boussinesq case $r = 0.7$. Figure 3(b) shows that the r -dependence in the right-moving front speed (2.7) produces an upward shift in $u^-(h)$ so that the intersection with the (unchanged) $u^+(h)$ shifts to $h_c \approx 0.3907$. Otherwise, the logic of the solution construction is identical to the Boussinesq case, and the now asymmetric spatial profile is illustrated in figure 4(b). The zone of constant state has shifted towards the right-moving front and has narrowed the right-side expansion fan. Again the analytical solution for $h(x/t)$ shown in the upper panel of figure 4(b) is identical with the SWE numerical solution shown in figure 2(b).

3.2.3. Non-Boussinesq case, $r = 0.4$

With further decreases in r , the right-side expansion fan is eventually eliminated at a critical value of r where $c_c^+ = u_R$. At this critical value of $r_{cr} (\approx 0.5821)$ the solution must undergo a change of spatial character. For $r < r_{cr}$, the intersection of the two Riemann invariant curves $u^+(h)$ and $u^-(h)$ occurs at an h -value that would be less than the value for the right-going characteristic Benjamin front (h_R) from (3.7). Specifically, the c_c^+ would exceed the propagation speed u_R of the assumed characteristic Benjamin front, which suggests that left-going rays are intersecting the right-moving front. The resolution is that the construction should now assume that the right-moving front parameters satisfy the time-like condition (3.8).

Figure 3(c) shows the $u^+(h)$ Riemann invariant curve extended to the value $h_R \approx 0.2725$ which, with $u_R \approx 0.8203$, also satisfies the Benjamin front condition (2.7). In the absence of the right-side expansion fan, the right-moving front conditions are now constant-state conditions. Figure 4(c) (lower panel) illustrates that the change to the time-like front is manifested by rays launched from the left-moving front catching up to the right-moving front. All rays of the c^- type carry constant values of h and u . As with the previous two cases the analytical solution for the height $h(x/t)$ in the upper panel of figure 4(c) matches the SWE numerical solution shown in figure 2(c).

The solution summary shown here in figure 5(a,b) agrees with the same shown in figure 15(a,b) of Ungarish (2011).

3.2.4. Summary and uniqueness of the causal solutions

A summary of the computed frontal values of h_R and u_R as a function of density ratio r are shown in figure 5. Free-boundary solutions for $r > r_{cr} \approx 0.5821$ have a characteristic Benjamin front, while for $r < r_{cr}$ have a time-like Benjamin front. As can be inferred from figure 4, there are two critical features that coincide at the value r_{cr} : (i) as $r \rightarrow r_{cr}$ from above, $c_c^+ \rightarrow u_R$ (right-going expansion fan disappears); and (ii) as $r \rightarrow r_{cr}$ from below, $c_R^+ \rightarrow u_R$ (rays emanating from left-going front become parallel to the right-going front).

The summary in figure 5 describes the unique causal solutions that are continuous on $v_L \leq x/t \leq u_R$, and assume a left-moving characteristic Benjamin front. To show that the present solutions are indeed unique we consider the hypothetical case of a left-moving time-like Benjamin front. This time-like front together with a right-moving time-like Benjamin front gives rise to a contradiction because both Riemann invariants $u^\pm(h)$ cannot satisfy the same end conditions $u^\pm(h_R) = u_R$ and $u^\pm(h_L) = u_L$ since an ODE inequality would follow from $c^-[u^-] \neq c^+[u^+]$. A left-moving time-like front together with a right-moving characteristic Benjamin front would require $c_L^- < v_L$ (rays emanating from right-moving front intersecting the left-moving front), which

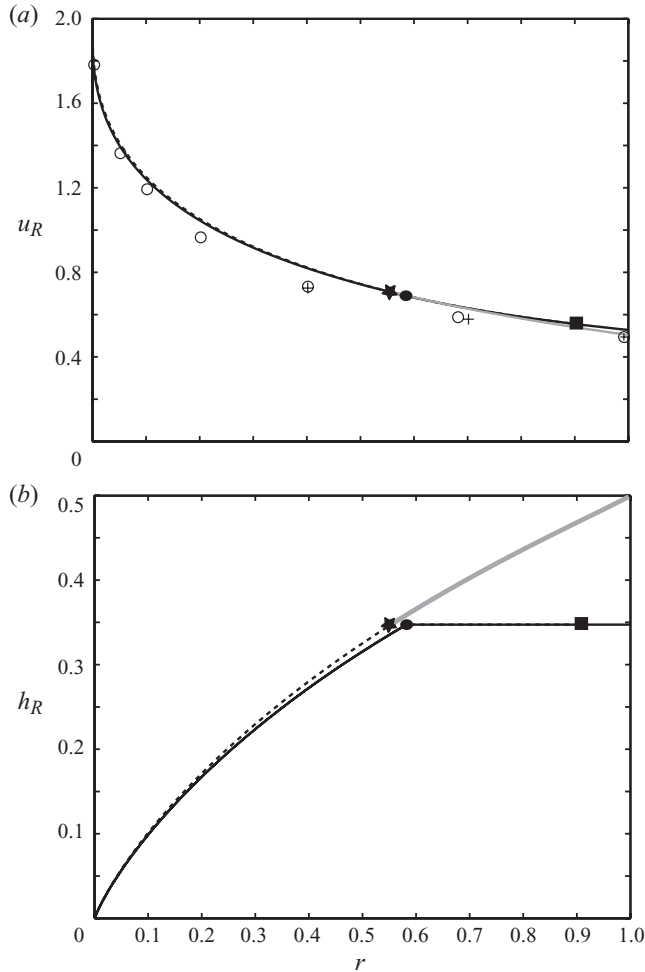


FIGURE 5. Right-moving front (a) speed u_R , and (b) height h_R , as a function of r . The present free-boundary solution (solid line) has two segments separated by the dot at $r = r_{cr} = 0.5821$ indicating the density ratio dividing characteristic ($r > r_{cr}$) from time-like ($r < r_{cr}$) Benjamin fronts. Solutions with the forced-boundary condition $u_L = h_L = 1/2$ and free-boundary conditions for the right-moving front (dashed line) have $r = r_{cr1} = 0.5532$ indicated by the star; the square at $r = r_{cr2} = 0.8953$ is the limiting density ratio beyond which continuous solutions do not exist for these assumed frontal conditions. The LRL solutions are same as the foregoing for $r < 0.5532$ but differ for $r > 0.5532$ (indicated by the solid grey line). The front-speeds from the present 2D and 3D numerical simulations are nearly identical and indicated by the ‘+’ symbol; data from the 2D simulations of Bonometti *et al.* (2008) are indicated by the circles.

is found to occur only for the unphysical parameter regime $r > (r_{cr})^{-1} > 1$. Thus, the characteristic solutions as described here are the unique continuous solutions.

3.3. Forced-boundary solutions

In this subsection we analyse the case considered by LRL of a dissipation-free left-moving front characterized by the particular front conditions

$$v_L = -u_L = -1/2, \quad d_L = h_L = 1/2, \quad (3.16)$$

satisfying the Benjamin relation (2.6). The wave speeds (2.4) associated with these conditions satisfy the inequality $v_L < c_L^- < c_L^+$, and hence both rays from the left-moving front are directed into the lock exchange region implying that the frontal motion is not influenced by the flow within the lock region. Therefore, from the point of view of the SWE, (3.16) violates ‘causality’ as defined above (for further discussion, see §4.2) and (3.16) must be considered a forced-boundary condition. Mathematically, the latter acts similarly to an initial condition and is commonly referred to as a *space-like* curve (Courant & Friedrichs 1948; John 1981, p. 28) as it shows two inbound rays in a ray diagram.

The construction of solutions to the SWE by the method of characteristics presented above is changed only in that conditions (3.12)–(3.13) are replaced by (3.16). For the range of values $0 \leq r < r_{cr1} \approx 0.5532$, the Riemann invariant analysis leads to the right-moving front being of the time-like Benjamin type. As seen in the example shown for $r = 0.4$ in figure 6(a), the spatial profile has a constant-state generated by the propagation of the left-moving dissipation-free front for $-1/2 < x/t < c_L^-$. The non-causal, hence forced, nature of this solution is evident in that both the c^+ and c^- rays are directed into the lock-exchange region. Otherwise, the spatial structure of the solution for $c_L^- < x/t < u_R$ is essentially like the free-boundary solution (figure 4c), consisting of an expansion fan and a constant-state following the right-moving front.

At larger values of $r_{cr1} < r < r_{cr2} \approx 0.8953$, the spatial profile of the solution again has a constant-state attached to the dissipation-free front followed by the two expansion fans typified by the right-moving characteristic Benjamin front case (e.g. figure 4b). This is illustrated for the case of $r = 0.7$ shown in figure 6(b). However, unlike the free-boundary solutions, there is a second critical value of $r_{cr2} \approx 0.8953$ where the central constant-state coincides with the dissipation-free-front conditions. This occurs where the Riemann invariant satisfies $u^-(1/2) = 1/2$. The implication of this for values of r approaching the Boussinesq case, $r_{cr2} < r \leq 1$, is that solutions would seem to require c^- rays that cross. Mathematically, this situation is typically resolved by the appearance of a shock or hydraulic jump. However, we choose not to pursue the analysis further, as our computations based on the NS equations (§4) suggest that the dissipation-free front is not realized at these larger values of r . The solution for $[u_R(r), h_R(r)]$ using the forced-boundary condition (3.16) is plotted on figure 5 as compared to the free-boundary solution. It is noted that the right-moving frontal parameters are little affected by this change in the left-moving front.

Finally, we consider the solution procedure described in LRL (their §3). LRL solve the Riemann invariant equation (3.3) for $u^+(h)$ starting from the left-moving condition (3.16) and look for a crossing with the Benjamin relation (2.7) to arrive at the right-moving frontal parameters (u_R, h_R) . For $r < r_{cr1}$ the LRL procedure is the same as the procedure that leads to the flow shown in figure 6(a). However, for $r > r_{cr1}$ we find that $c_c^+ < u_R$ implying that rays emanating from the left-moving front do not reach the right-moving front; hence in our construction of the solution for this case, the left-going rays from the right-moving characteristic Benjamin front are necessary to complete the solution through the right-side expansion fan (figure 6b). Although it is possible to construct the solution for $r > r_{cr1}$ (figure 6c) following the LRL procedure, one would need some physical basis external to the SWE for assigning the derived frontal parameters (u_R, h_R) which now must also be considered a forced-boundary condition. In the limit as $r \rightarrow 1$, the LRL procedure produces the solution $u = h = 1/2$ for $-1/2 < x/t < +1/2$ (LRL, their figures 11–12) and versions of the latter may be found in the literature dating back to the 1940s (Yih 1965, pp. 134–138).

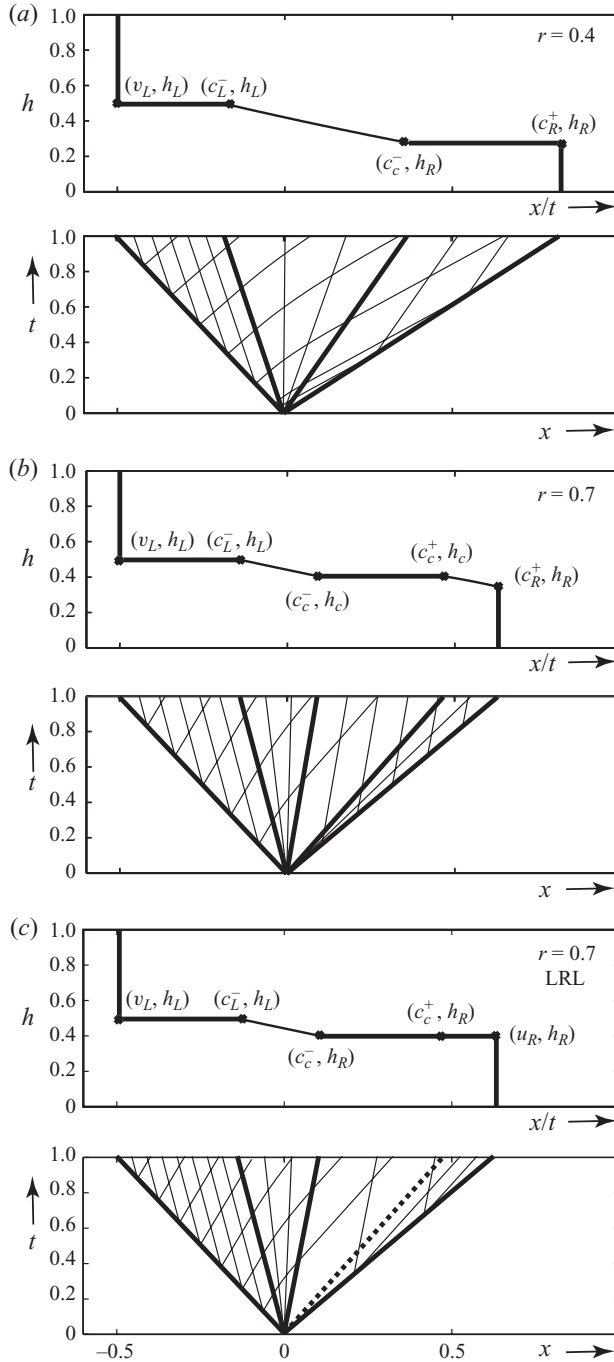


FIGURE 6. Analytical construction of the solution to the shallow water equations for the forced boundary condition $u_L = -v_L = h_L = 1/2$ and free-boundary conditions on the right-moving front for (a) $r=0.4$, (b) $r=0.7$ and (c) the LRL solution for $r=0.7$ with forced-boundary conditions at both left and right fronts.

Nevertheless, as shown in figure 5, there is little difference in $u_R(r)$ produced by the present, the modified LRL or the LRL solutions to the SWE; the major difference is in $h_R(r)$ for $r_{cr} < r < 1.0$.

4. Numerical simulations

To assess the solutions of the two-layer SWE presented in the previous sections, we proceed here to more general equations of fluid motion. In the present work we follow Étienne *et al.* (2005), who give the equations of motion for a mixture of two incompressible fluids of different densities. The fluid density is given by $\tilde{\rho} = \rho_h \Phi + \rho_l(1 - \Phi)$ or non-dimensionalizing by the density of the heavier fluid ρ_h , $\rho = r + (1 - r)\Phi$, where Φ is the heavier-fluid volume fraction and ρ_l is the density of the lighter fluid. Using the same non-dimensionalization as used for the shallow-water equations in §2, the equations expressing conservation of mass of the mixture, mass of the denser fluid and momentum of the mixture are, respectively,

$$\frac{\partial u_i}{\partial x_i} = -\frac{(1-r)}{r+(1-r)\Phi} \frac{D\Phi}{Dt}, \quad (4.1)$$

$$\frac{D\Phi}{Dt} + \Phi \frac{\partial u_i}{\partial x_i} = \frac{1}{ReSc} \frac{\partial^2 \Phi}{\partial x_i^2} \quad (4.2)$$

and

$$\rho \frac{Du_i}{Dt} = -\frac{\partial p}{\partial x_i} + \frac{2}{Re} \frac{\partial}{\partial x_j} \left[\lambda(\Phi) \left(e_{ij} - \frac{1}{3} \frac{\partial u_k}{\partial x_k} \delta_{ij} \right) \right] - \frac{\rho}{1-r} \delta_{i3}, \quad (4.3)$$

where $Re = \rho_h UH/\eta$ and $Sc = (\eta/\rho_h)/\kappa$ are respectively the Reynolds and Schmidt numbers, η is a constant reference value for the dynamic viscosity, κ is the diffusion coefficient (assumed constant) and $U = \sqrt{(1-r)gH}$. Étienne *et al.* (2005) let the dynamic viscosity $\mu = \eta\lambda(\Phi)$ to allow for either constant dynamic viscosity ($\lambda = 1$) or constant kinematic viscosity [$\lambda = r + (1-r)\Phi$].

Seeking solutions that are as close as possible to the physical situation described by the two-layer SWE, we will focus on the limiting case $Sc \rightarrow \infty$, signifying zero cross-species diffusion. With the assumption of constant dynamic viscosity, (4.1)–(4.3) simplify to

$$\frac{\partial u_i}{\partial x_i} = 0, \quad (4.4)$$

$$\frac{D\rho}{Dt} = 0 \quad (4.5)$$

and

$$\rho \frac{Du_i}{Dt} = -\frac{\partial p}{\partial x_i} + \frac{1}{Re} \frac{\partial^2 u_i}{\partial x_j^2} - \frac{\rho}{1-r} \delta_{i3}. \quad (4.6)$$

Equations (4.4)–(4.6) are the same as solved by Bonometti *et al.* (2008) where it is noted (p. 451) that there is in effect a finite value of $Sc \approx O(10^3)$ due to the limitations of finite-differencing across the sharp change in ρ at the fluid–fluid interface. Again, in conformity with the SWE, we will assume stress-free conditions at the upper and lower boundaries. Hereinafter, (4.4)–(4.6) are referred to as the NS equations.

As noted in the Introduction and in previous work, the interface separating the heavier- from the lighter-fluid flows is generally unstable; hence one expects a transition to turbulence beyond some threshold value of Re , and therefore, turbulent

stress and species diffusion between the two fluids. To avoid turbulent stresses and species diffusion, one might restrict attention to lower- Re (laminar) cases; however, for a low- Re flow there would then be viscous stress between the two fluids. Hence, stress between the fluids is a generally unavoidable difference between the NS and the SWE solutions for lock-exchange flow. In the present paper, we will present solutions ranging from turbulent to laminar flow. Although the lock (figure 1) is in principle two-dimensional, turbulent motion is fundamentally three-dimensional and therefore we will explore solutions to (4.4)–(4.6) for variations in (r, Re) in both two and three dimensions. Details on the numerical-solution technique, grid resolution, solution verification, etc. are given in the Appendix.

4.1. Results and comparison with the SWE solutions

To facilitate comparison of the SWE solutions (§3) with the NS solutions, it is convenient to plot the latter as a function of x/t at a time long enough for the establishment of a statistically steady-state solution and non-hydrostatic effects associated with the initial evolution will be absent. Plotted in this way, long-wave features of the NS solutions stand out more clearly, and shorter-wave features such as the leading-edge gravity currents are compressed, analogous to the way they are represented in the SWE. Figures 7(a), 7(c) and 7(e) show the density field $\rho(x/t, z)$ from two-dimensional simulations of the cases $r = 1.0, 0.7$ and 0.4 , respectively, with $Re = 10^4$, while figures 7(b), 7(d) and 7(f) show the y -averaged density field $\bar{\rho}(x/t, z)$ from three-dimensional simulations for the same cases (all at $t = 16$). Beginning with the Boussinesq case $r = 1$, figure 7(a) indicates flow instability along the interface between the advancing fronts; however, without the ability to produce a turbulent cascade to smaller scales, the flow is dominated by large-scale ‘billows’. In three dimensions, figure 7(b) shows that the two-dimensional instability is able to break down into three-dimensional turbulence which diffuses the interface. For the non-Boussinesq case $r = 0.7$, the two- and three-dimensional simulations in figures 7(c) and 7(d), respectively, also indicate turbulent flow along the interface with a suggestion of a reduced level of turbulence for the left-moving front. However for $r = 0.4$, the two- and three-dimensional simulations in figures 7(e) and 7(f), respectively, indicate laminar flow for the left-moving front and turbulent flow for the right-moving front. This simulated disappearance of turbulence from the left-moving front with decreasing r has been found in the laboratory and numerical studies reviewed in §1. Overlaid on the three-dimensional numerical solutions are the present and the LRL solutions to the SWE. Some general points of comparison follow.

Both the present and the LRL solutions of the SWE agree with the NS solutions in that the speed of the left-moving front is independent of r while that of the right-moving front is inversely proportional to r (the NS $u_R(r)$ data points, plotted in figure 5a, are generally slower than the SWE solutions); the NS solutions all have $v_L \approx -0.5$ as in the LRL SWE solution as compared with $v_L = -0.527$ in the present SWE solution. The present SWE solution agrees with the NS solutions in that the interface generally slants from the upper left to the lower right in all cases while the LRL solution approaches a level interface as $r \rightarrow 1$. In both SWE solutions, the right-moving front thins with decreasing r in agreement with the NS solution. We note that the only ‘zone of constant state’ that clearly emerges in the NS solutions is the one attached to the left-moving front for $r = 0.4$ in agreement with the LRL solution; otherwise the NS solutions exhibit an interface that slopes from upper left to lower right approximately linearly in the variable x/t . Denoting the height of the middle density contour by \hat{h} and letting $\eta = x/t$, this linear dependence can be

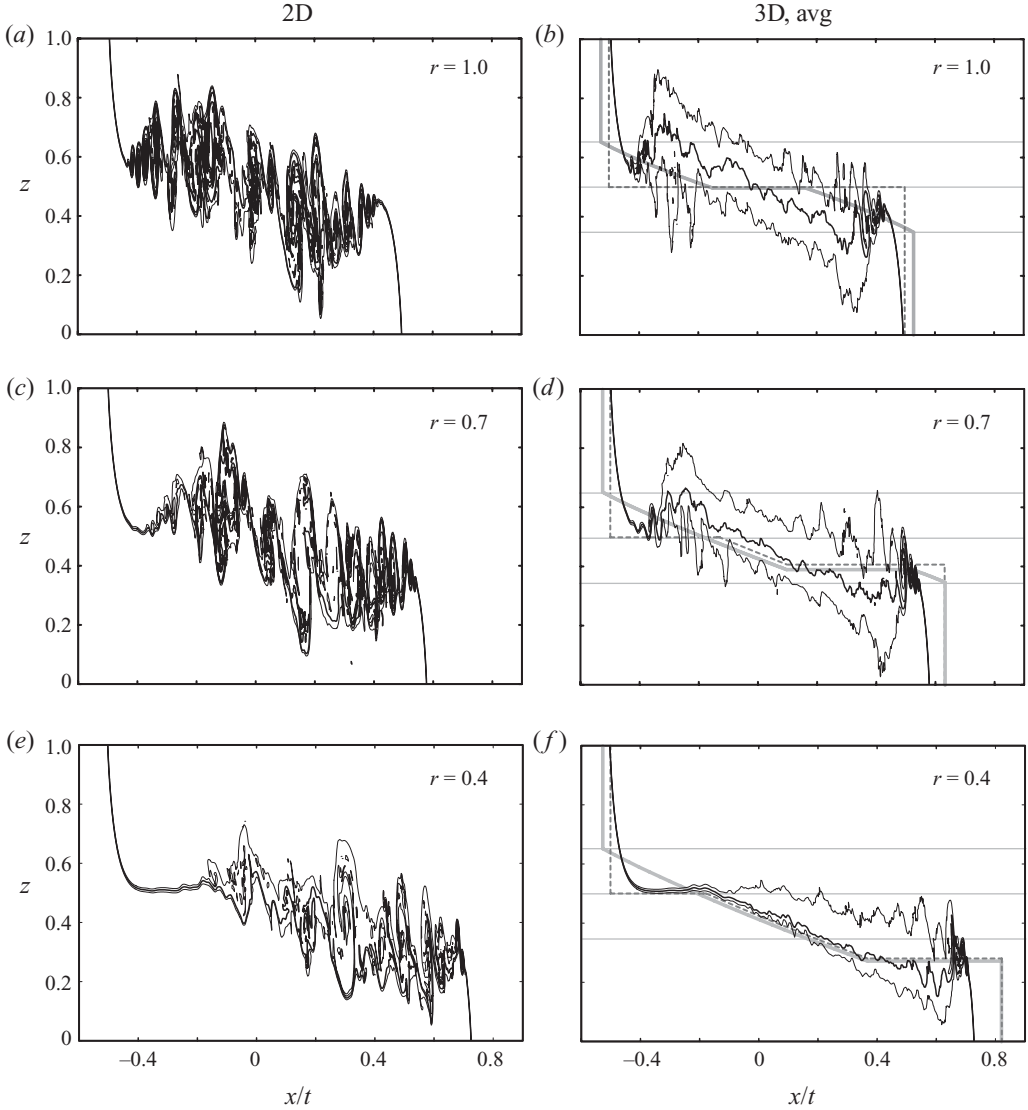


FIGURE 7. Navier–Stokes simulations of lock-exchange flow in two dimensions for density ratios $r=(a)$ 1.0, (c) 0.7 and (e) 0.4 and in three dimensions for $r=(b)$ 1.0, (d) 0.7 and (f) 0.4. Shown from the three-dimensional simulations is the y -averaged density field. The three contour intervals displayed in all plots are 0.1, 0.5 and 0.9, with the middle value emphasized. Overlaid on the three-dimensional solutions are the present solutions to the SWE (solid grey line) and those proposed by LRL (dashed grey line). The three horizontal grey lines in (b) , (d) and (f) mark $z=0.3473$, 0.5 and 0.6527.

expressed as

$$\hat{h}(\eta) = \hat{h}_L - (\hat{h}_L - \hat{h}_R) \frac{\eta - \eta_L}{\eta_R - \eta_L}. \quad (4.7)$$

Although it is difficult to unambiguously identify the parameters in (4.7) from the NS solutions, it seems clear that, for these solutions with $Re = 10^4$, \hat{h}_L decreases with r , reaching the asymptotic limit $\hat{h}_L = 1/2$ between $r=0.7$ and $r=0.4$.

4.2. Discussion

In our judgement, the foregoing NS–SWE-solution comparison indicates only limited success for the SWE solutions. This comparison is complicated by the presence in the NS solutions of turbulent eddies along the unstable interface between the two fluid layers and the consequent mixing that tends to smooth the sharp transitions found in the SWE solutions. The one place where turbulence is suppressed in the NS solutions is in the region behind the left-moving front for $r=0.4$ and here, the solution compares favourably with the LRL SWE solution. However, even in this case it must be recalled that the condition (3.16) is externally ‘forced’ in that there are no characteristic curves that reach the event line $x/t = -0.5$ from the lock region (see figure 6c). In the NS solution the evolving interface is obviously a free boundary as information must come from the lock region. One can reasonably infer that local non-hydrostatic effects must produce a propagation speed faster than that supported by the SWE for the conditions (3.16); however, a more precise mathematical model for this effect is unknown to the authors.

Accepting that there is an inherent tendency for the left-moving front to satisfy the conditions (3.16) for small r , we investigate the conditions under which this occurs in the NS simulations. The tendency $\hat{h}_L(r) \rightarrow 1/2$ with decreasing r is also accompanied by a decrease in instability and turbulence at the left-moving front (figure 7). These results suggest a transition with decreasing r from an NS solution more akin to the present SWE solution ($h_L = 0.6527$ at a dissipative Benjamin front) to one more akin to the LRL SWE solution ($h_L = 0.5$ at a dissipation-free Benjamin front). To reinforce the point, we show in figure 8(a–f) $\rho(x, z)$ and $\bar{\rho}(x, z)$ respectively from the present two- and three-dimensional simulations (at $t = 16$) with $Re = 10^4$ windowed in on the left-moving front together with the Benjamin potential-flow solution (Benjamin 1968, his §4.3). Figure 8(a) shows that the flow is unstable at $(r, Re) = (1.0, 10^4)$; the ensuing turbulence, upon an across-flow average (figure 8b), indicates that the middle density contour lies close to the present theoretically predicted $h_L = 0.6527$. Figure 8(c) indicates a more gradually developing instability at $(r, Re) = (0.7, 10^4)$; figure 8(d) shows that turbulent mixing occurs farther downstream but nonetheless indicates a middle density contour close to $h_L = 0.6527$. Figure 8(e–f) indicates that at $(r, Re) = (0.4, 10^4)$ the flow is stable and consequently without turbulence; in this case the NS solutions closely approximate the Benjamin potential-flow solution and one would judge $h_L = 0.5$. Hence, we conclude that \hat{h}_L will be controlled by the instability at the left-moving front. The calculations in figure 8(a–f), carried out at $Re = 10^4$, show that turbulence is suppressed at the left-moving front for $r = 0.4$; however figure 8(g) shows that increasing the Reynolds number to $Re = 5 \times 10^4$ for this case of $r = 0.4$ indicates instability at the left-moving front. Hence, there is a strong indication from the present NS solutions that the character of the left-moving front depends on both Re and r . Figure 9 shows the entire flow for $(r, Re) = (0.4, 5 \times 10^4)$ plotted as in figure 7 and it is clear that the instability at the leading edge of the left-moving front brings its shape closer to the present SWE solution than to the LRL SWE solution.

For $r \approx 1$ theory indicates that the upper left-moving current is unstable to disturbances of all wavelengths, but that as r decreases from unity, the longest wavelengths are stabilized (Benjamin 1968, pp. 224–225 and figure 15(a) of LRL). Since viscous effects are strongest at the shorter wavelengths, and since longer wavelengths become stable for $r < 1$, instability is suppressed for combinations of smaller r and smaller Re ; the evidence from figure 8(e) is that viscous effects are large enough to suppress turbulence but not large enough to cause major departures from Benjamin’s potential-flow solution for $r = 0.4$ and $Re = 10^4$.

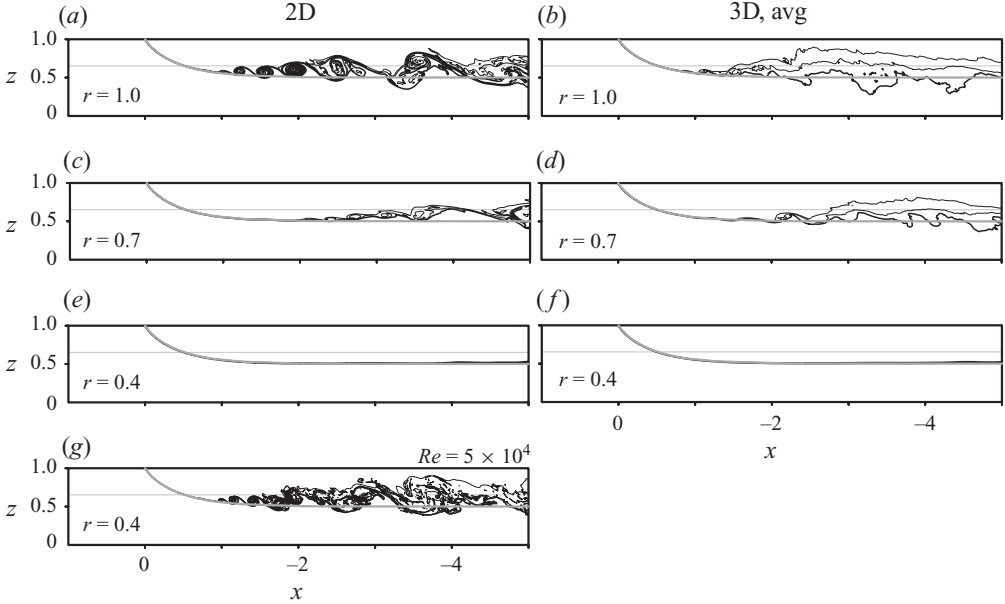


FIGURE 8. Density field (contours=0.1, 0.5 and 0.9) plotted as a function of the distance relative to the left-moving front at $t=16$ from two- and three-dimensional Navier–Stokes simulations of lock-exchange flow with (a) $r=1.0$, 2D, (b) $r=1.0$, 3D avg, (c) $r=0.7$, 2D, (d) $r=0.7$, 3D avg, (e) $r=0.4$, 2D and (f) $r=0.4$, 3D avg with $Re=10^4$ in all cases. As in (e), panel (g) has $r=0.4$, 2D but $Re=5 \times 10^4$. Overlaid in all panels is the interface as computed from Benjamin’s potential-flow solution. The horizontal grey line denotes $h_L=0.6527$ for the left-moving front according to the present theory.

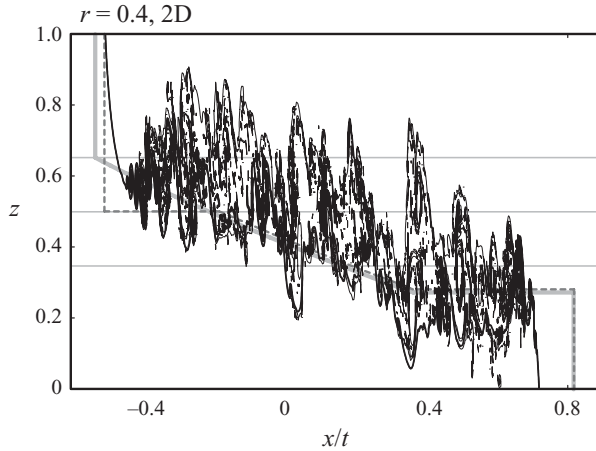


FIGURE 9. As in figure 7(e), except for $Re=5 \times 10^4$; analytical solutions overlaid as in figure 7(f).

The right-moving frontal parameter $u_R(r)$ (figure 5a) from any of the SWE solutions compares rather well with the present NS solutions as well as those produced in 2D simulations by Bonometti *et al.* (2008) over a wider range of r . There is, however, significant disagreement between the present model and the LRL model right-moving frontal parameter $h_R(r)$ for $r > r_{cr1}$ where the latter produces $h_R \rightarrow 1/2$ as $r \rightarrow 1$. For the Boussinesq case, we believe the present model is closer to the NS solution in that

figure 7(b) shows a significant overall tilt (from upper left to lower right) of $h(x/t)$ rather than the level interface $h(x/t) = 1/2$ predicted in the LRL SWE solution (see their figure 12 with $r = 1$).

5. Summary and conclusions

Although the general sense of the circulation in lock-exchange flow is easily deduced from the initial baroclinic distribution of density and pressure, more precise detail on the motion and nature of the evolving interface requires a fluid-flow model. In the present work we reviewed and advanced analytical models based on the shallow-water equations for non-Boussinesq lock-exchange flow. These analytical models were then compared with their counterpart numerical solutions based on the (NS) equations.

Nearly all of the existing analytical models of non-Boussinesq lock-exchange flow are based on the shallow-water approximation. Since the latter approximation fails near the leading edges of the mutually intruding flows (figure 1), front conditions must be given at both left- and right-moving fronts in order to find solutions to the shallow-water equations. That a variety of such solutions exist in the literature is due to the individual investigators choice of front conditions (e.g. KRS and LRL); furthermore permitting discontinuous solutions between the two fronts gives an even greater variety of solutions (e.g. KC; see figure 4a of LRL). In KRS, the shallow-water equations were solved numerically for the Boussinesq lock-exchange problem under the conditions that the left- and right-moving fronts satisfy the Benjamin front conditions (2.6) and (2.7), respectively, and that the front is a free boundary influenced by the motion within the lock region (i.e. it obeys ‘causality’). The present paper has extended the KRS numerical solutions to cover non-Boussinesq flows (figure 2).

Using the method of characteristics, we have found exact analytical solutions (figures 3–5) that verify the numerical solutions of the shallow-water equations given here and in KRS. They also reinforce the finding that only solutions with frontal parameters implying dissipation at the fronts obey ‘causality’ in the shallow-water equations. However, it has been noted in both laboratory and numerical experiments that the left-moving front becomes less dissipative, taking the form of a potential-flow solution found by Benjamin (1968), as r , the ratio of lighter- to heavier-fluid density, decreases. Following LRL we have found analytical solutions of the shallow-water equations by imposing the dissipation-free condition on the left-moving front. As noted in KRS, the dissipation-free front moves at a speed greater than the shallow-water-equation wave speed and hence, from the point of view of shallow-water theory, must be considered a forced-boundary condition. For $r < r_{cr1} = 0.5532$, our solutions assuming a left-moving dissipation-free front have rays emanating from the left-moving front that impinge on the right-moving front and thus determine the right-moving frontal parameters; these solutions are the same as those of LRL (figure 6a). For $r > r_{cr1}$, we find that rays emanating from the left-moving front do not reach the right-moving front and that the solution must be completed with a right-going expansion fan (figure 6b). Notwithstanding that the left-going rays do not reach the right-moving front for $r > r_{cr1}$, LRL continue to look for the intersection of the solution to the Riemann invariant equation (3.3) with the Benjamin front condition (2.7) to find the right-moving frontal parameters; we have constructed analytical solutions (figure 6c), with the understanding that these must be regarded as solutions in which both the left- and right-moving frontal parameters represent forced-boundary conditions.

In an attempt to authenticate the various solutions to the shallow-water equations, we have carried out both two- and three-dimensional numerical solutions of the

NS equations for relatively large Reynolds number ($Re = 10^4$), very large Schmidt number ($Sc \gg 1$) and free-slip conditions at the upper and lower bounding surfaces. For $Re = 10^4$ and $r = 1$, the interface separating lighter and heavier fluid is generally turbulent; however, as found in recent numerical studies, the left-moving front becomes less turbulent with decreasing r . In the present simulations with $Re = 10^4$, the left-moving front is essentially laminar at $r = 0.4$ (figure 7*e, f*) and closely approximates the Benjamin potential-flow solution (figure 8*c*). A further experiment keeping $r = 0.4$ but with a larger Re shows that the left-moving front is again turbulent (figure 9) suggesting there is a dependence on both Re and r that determines the character of the left-moving front.

Comparison of the present (free-boundary) with the LRL (forced-boundary) solutions of the shallow-water equations with their counterpart numerical solution of the NS equations produced mixed results. Both the free and forced solutions reproduced the NS-solution features of left-moving frontal parameters (v_L, d_L) independent of r , right-moving front speed u_R increasing with r and right-moving front height h_R decreasing with r . The present free-boundary theory produced $v_L = -0.527$ while the forced-boundary theory prescribed $v_L = -0.5$ which agrees closely with the NS solutions. On the other hand, in the limit as $r \rightarrow 1$, the forced-boundary theory gives the level interface $h(x/t) = 0.5$ between the left- and right-moving fronts, while the present free-boundary theory gives an interface that is tilted from lower right to the upper left implying that both d_L and h_L are less than 0.5 in agreement with the NS solutions. We noted that the only place where the NS solutions produced a zone of constant state is in association with the left-moving front for relatively small r and Re . Both free- and forced-boundary theories gives very similar predictions for $u_R(r)$ which in turn compared well with the NS solutions.

In the generally non-hydrostatic NS solutions, the evolving interface is of course a free boundary whose motion must be influenced by the flow in the lock region. We are unaware of an analytical theory taking account of non-hydrostatic effects and a density interface intersecting the rigid surfaces that can be used to explain the evolution from $t = 0$ to the time when the steadily propagating fronts are established in lock-exchange flow. In addition to explaining how information flows from the lock region to the fronts, such a theory may also shed light on why the the upper-front speed $v_L \approx -0.5$ across the range of r while the upper-front h_L clearly varies with r in the NS solutions (figure 7). It may also explain why NS front speeds are relatively insensitive to the interfacial dynamics – both two- and three-dimensional simulations (with very different versions of interfacial turbulence) give surprisingly similar predictions for the front speeds (figure 5*a*).

D. J. M. is supported through NSERC RGPIN-238928. The National Center for Atmospheric Research is sponsored by the National Science Foundation.

Appendix. Details of the Navier–Stokes solver

Numerical integration of the NS equations (4.4)–(4.6) requires solution of an elliptic equation to determine pressure p . Solution techniques can be expensive in three dimensions with resolution high enough for adequately resolved direct numerical simulation (DNS) and can be difficult to implement effectively on modern distributed-memory computing systems. As an alternative, we replace the mass-continuity equation (4.4) with a prognostic equation for pressure. This procedure eliminates the need to solve an elliptic equation, but introduces the need to account

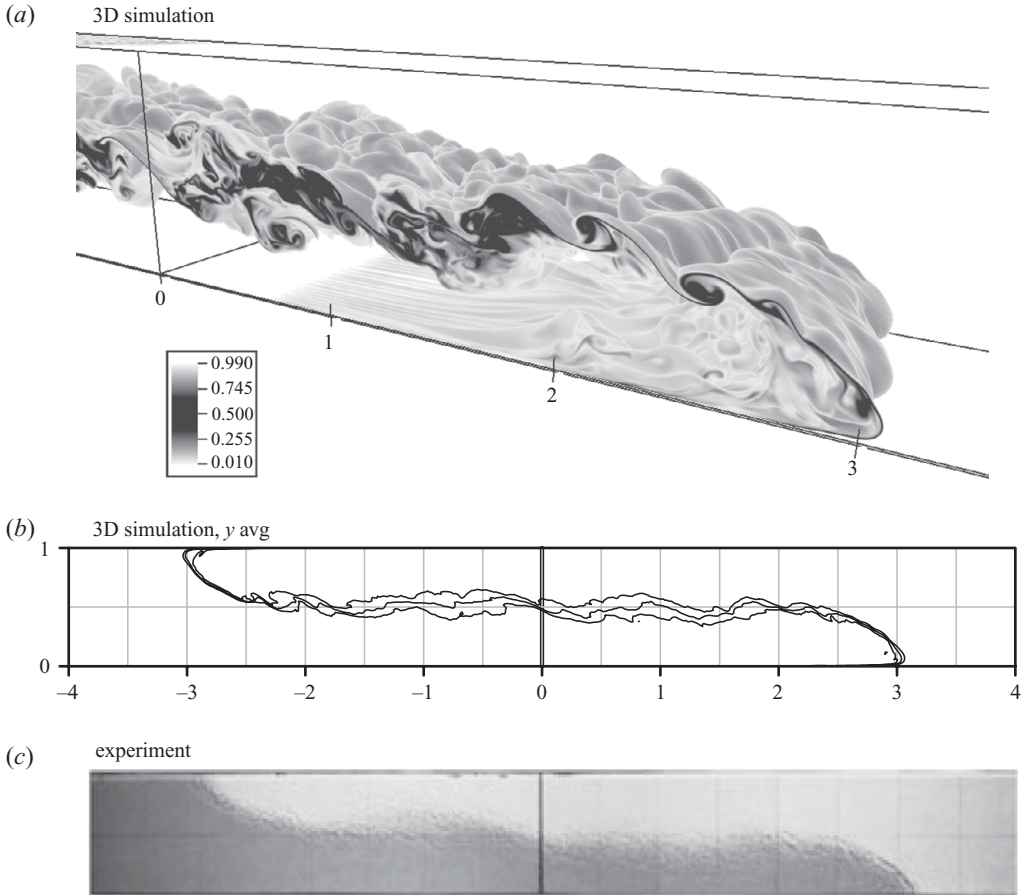


FIGURE 10. Direct numerical simulation of a Boussinesq lock-exchange laboratory experiment at $t = 7$ showing a rendition of the middle density surfaces (a), an across-channel average of the density field (b, contours = 0.25, 0.50 and 0.75) and a shadowgraph image from the laboratory experiment of Shin *et al.* (2004, c).

for acoustic waves. The latter problem is addressed in the present study using the procedure developed by Klemp, Skamarock & Dudhia (2007). Our derivation of an appropriate pressure equation follows Chorin (1967); herein, we assume p is a function of ρ only, and we invoke an artificial speed of sound $c_s \equiv dp/d\rho$, then using (4.4)–(4.5) we find

$$\frac{Dp}{Dt} = -\rho c_s^2 \frac{\partial u_i}{\partial x_i}. \quad (\text{A } 1)$$

We set $c_s = 10\sqrt{g'H}$ to ensure that acoustic waves propagate much faster than the flow in the parameter space investigated herein ($r \geq 0.05$).

The time-integration method is third-order Runge–Kutta using time-split integration for acoustic terms following Wicker & Skamarock (2002). Advection terms are calculated using the sixth-order flux-form discretization of Wicker & Skamarock (2002), and all other spatial derivatives are calculated using second-order centred discretization. Further details are available in Bryan & Rotunno (2008, p. 548), although herein the subgrid turbulence parameterization of KRS is replaced

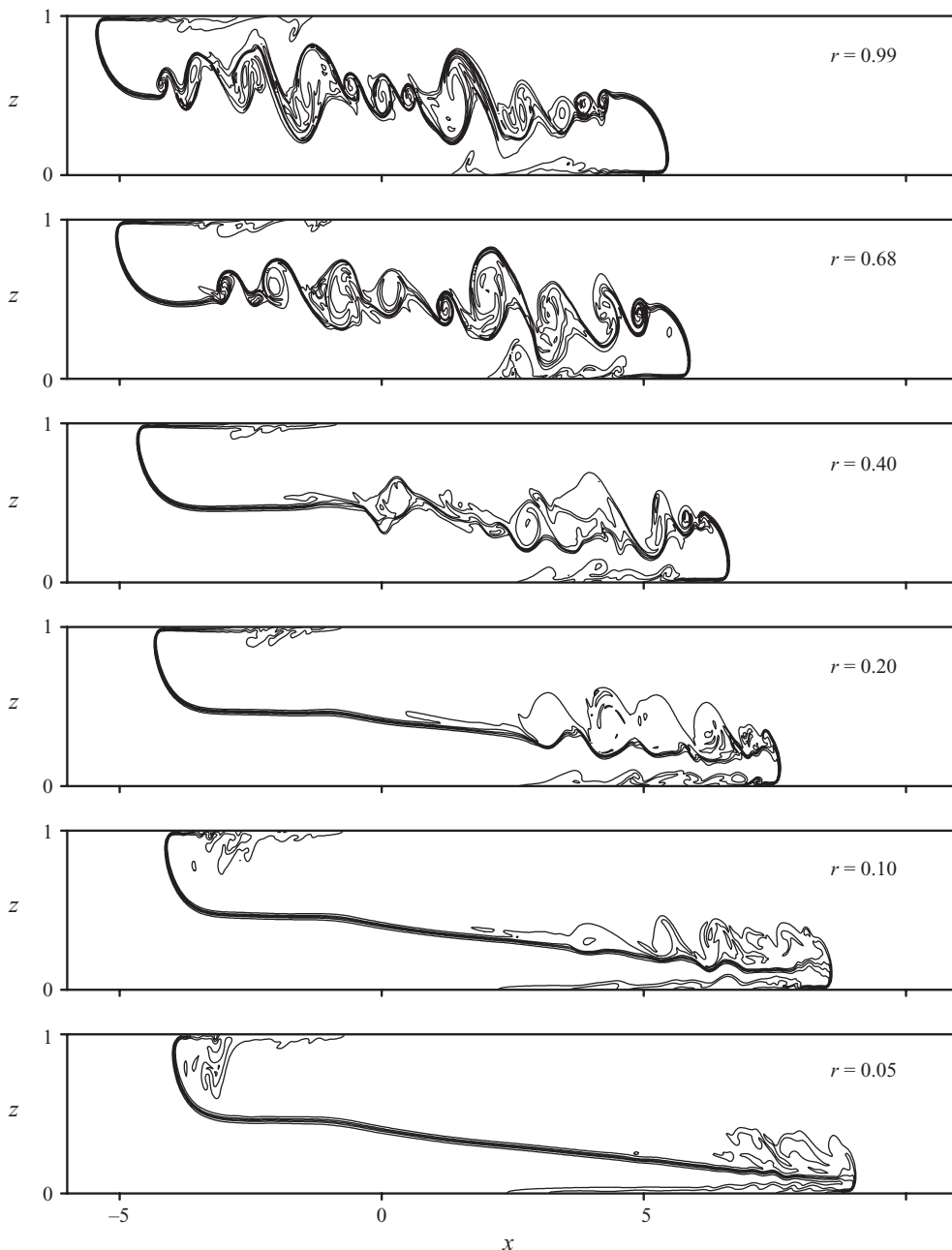


FIGURE 11. Simulation results using the same settings as in figure 4 of Bonometti *et al.* (2008).

by explicit stress-divergence calculations (second term on right side of (4.6)). The domain extends from $x = -9$ to $x = +9$ for $r = 0.99$, from $x = -9$ to $x = +11$ for $r = 0.7$ and from $x = -9$ to $x = +13.5$ for $r = 0.4$. The initial 'lock' is located at $x = 0$. All simulations extend from $y = 0$ to $y = 1$ and $z = 0$ to $z = 1$. The grid spacing is $1/320$ in all directions for all simulations except the the two-dimensional simulation shown in figures 8(g) and 9 where it was decreased to $1/960$. Following previously

published guidelines for consistency in DNS between resolution and Re (Moin & Mahesh 1998, §2.1), this resolution is considered sufficient for our nominal setting $Re = 10^4$ and the one special simulation with $Re = 5 \times 10^4$.

Pressure at $t = 0$ is determined using (4.4) and (4.6). Because $u_i(t = 0) = 0$ everywhere and $\rho(t = 0)$ is a function of x only, then the elliptic equation that applies at $t = 0$ is

$$\frac{\partial^2 p}{\partial x^2} - \frac{1}{\rho} \frac{\partial \rho}{\partial x} \frac{\partial p}{\partial x} + \frac{\partial^2 p}{\partial z^2} = 0, \quad (\text{A } 2)$$

which is solved using successive over-relaxation.

To allow for development of three-dimensional motion in 3D simulations, small-amplitude random horizontal-velocity perturbations are added to the initial state. Slightly higher amplitude perturbations are inserted at $|x| < 0.1$ to crudely replicate laboratory experiments in which turbulent motions are created by abrupt removal of a partition at $t \approx 0$.

The solver is evaluated in two ways: comparison against a laboratory result and comparison against previously published numerical simulations. For the first evaluation, we run a three-dimensional simulation and compare against the Boussinesq lock-exchange experiment of Shin *et al.* (2004, their figure 2). Our numerical simulation uses $r = 0.99$ and $Re = 10^4$, similar to values for the experiment of Shin *et al.* (2004). No-slip boundary conditions are used for this simulation. Results at $t = 7$ are shown in figure 10, wherein figure 10(a) shows a view of the height of the middle density surface and figure 10(b) shows $\bar{\rho}(x, z)$ from the numerical simulation; figure 10(c) shows the shadowgraph image from Shin *et al.* (2004). The numerical simulation clearly captures the salient features of the experiment such as the propagation speed of the fronts, turbulent mixing along the interface and a sloped interface at $x = 0$.

For comparison against previously published results, we simulate two-dimensional lock-exchange flow across a large range of r following Bonometti *et al.* (2008). For these simulations we use the same settings as Bonometti *et al.* (2008): a domain of 25×1 ; $\Delta z = 1/160$; $\Delta x = 1/64$ and no-slip boundary conditions. Bonometti *et al.* (2008) used a different method for non-dimensionalization than we use herein; to allow direct comparison to their results we use $Re = 7071\sqrt{1+r}$ and we examine the output at $t = 9\sqrt{1+r}$. Results in figure 11 are comparable to those from Bonometti, Blachandar & Magnaudet (2008, their figure 4) in terms of the overall structure and front propagation speeds.

REFERENCES

- BENJAMIN, T. B. 1968 Gravity currents and related phenomena. *J. Fluid Mech.* **31**, 209–248.
- BIRMAN, V., MARTIN, J. E. & MEIBURG 2005 The non-Boussinesq lock-exchange problem. Part 2. High resolution simulations. *J. Fluid Mech.* **537**, 125–144.
- BONOMETTI, T., BLACHANDAR, S. & MAGNAUDET, J. 2008 Wall effects in non-Boussinesq density currents. *J. Fluid Mech.* **616**, 445–475.
- BRYAN, G. H. & ROTUNNO, R. 2008 Gravity currents in a deep anelastic atmosphere. *J. Atmos. Sci.* **65**, 536–556.
- CHORIN, A. J. 1967 A numerical method for solving incompressible viscous flow problems. *J. Comput. Phys.* **2**, 12–26.
- CHUMAKOVA, L., MENZAQUE, F. E., MILEWSKI, P. A., ROSALES, R. R., TABAK, E. G. & TURNER, C. V. 2009 Stability properties and nonlinear mappings of two- and three-layer stratified flows. *Stud. Appl. Maths* **122**, 123–137.
- COURANT, R. & FRIEDRICHS, K. O. 1948 *Supersonic Flow and Shock Waves*. Springer.
- ÉTIENNE, J., HOPFINGER, E. & SARAMITO, P. 2005 Numerical simulations of high density ratio lock-exchange flows. *Phys. Fluids* **17**, 036601.

- GRÖBELBAUER, H. P., FANNELOP, T. K. & BRITTER, R. E. 1993 The propagation of intrusion fronts of high density ratios. *J. Fluid Mech.* **250**, 669–687.
- HÄRTEL, C., MEIBURG, E. & NECKER, F. 2000 Analysis and direct numerical simulation of the flow at a gravity current head. Part 1. Flow topology and front speed for slip and no-slip boundaries. *J. Fluid Mech.* **418**, 189–212.
- JOHN, F. 1981 *Partial Differential Equations*. Springer.
- KELLER, J. J. & CHYOU, Y.-P. 1991 On the hydraulic lock-exchange problem. *J. Appl. Math. Phys.* **42**, 874–910.
- KLEMP, J. B., ROTUNNO, R. & SKAMAROCK, W. C. 1994 On the dynamics of gravity currents in a channel. *J. Fluid Mech.* **269**, 169–198.
- KLEMP, J. B., SKAMAROCK, W. C. & DUDHIA, J. 2007 Conservative split-explicit time integration methods for the compressible nonhydrostatic equations. *Mon. Weath. Rev.* **135**, 2897–2913.
- LOWE, R. J., ROTTMAN, J. W. & LINDEN, P. F. 2005 The non-Boussinesq lock-exchange problem. Part 1. Theory and experiments. *J. Fluid Mech.* **537**, 101–124.
- MOIN, P. & MAHESH, K. 1998 Direct numerical simulation: A tool in turbulence research. *Annu. Rev. Fluid Mech.* **30**, 539–578.
- ROTTMAN, J. W. & SIMPSON, J. E. 1983 Gravity currents produced by instantaneous releases of a heavy fluid in a rectangular channel. *J. Fluid Mech.* **135**, 95–110.
- SHIKHMURAZAEV, Y. D. 2008 *Capillary Flows with Forming Interfaces*. Chapman and Hall/CRC.
- SHIN, J. O., DALZIEL, S. & LINDEN, P. F. 2004 Gravity currents produced by lock exchange. *J. Fluid Mech.* **521**, 1–34.
- SIMPSON, J. E. & BRITTER, R. E. 1979 The dynamics of the head of a gravity current advancing over a horizontal surface. *J. Fluid Mech.* **94**, 477–495.
- UNGARISH, M. 2007 A shallow-water model for high-reynolds-number gravity currents for a wide range of density differences and fractional depths. *J. Fluid Mech.* **579**, 373–382.
- UNGARISH, M. 2008 Energy balances and front speed conditions of two-layer models for gravity currents produced by lock release. *Acta Mechanica* **201**, 63–81.
- UNGARISH, M. 2009 *An Introduction to Gravity Currents and Intrusions*. CRC Press.
- UNGARISH, M. 2010 Energy balances for gravity currents with a jump at the interface produced by lock release. *Acta Mechanica* **211**, 1–21.
- UNGARISH, M. 2011 Two-layer shallow-water dam-break solutions for non-Boussinesq gravity currents in a wide range of fractional depth. *J. Fluid Mech.* **675**, 27–59.
- WHITHAM, G. B. 1974 *Linear and Nonlinear Waves*. Wiley.
- WICKER, L. J. & SKAMAROCK, W. C. 2002 Time-splitting methods for elastic models using forward time schemes. *Mon. Weath. Rev.* **130**, 2088–2097.
- YIH, C.-S. 1965 *Dynamics of Nonhomogeneous Fluids*. Macmillan.